Ceramics International 46 (2020) 7430–7437

Contents lists available at ScienceDirect

Ceramics International

journal homepage: www.elsevier.com/locate/ceramint

Microstructure and dielectric properties of high entropy Ba($Zr_{0.2}Ti_{0.2}Sn_{0.2}Hf_{0.2}Me_{0.2}$)$O_3$ perovskite oxides

Shiyu Zhou, Yongping Pu*, Qianwen Zhang, Ruike Shi, Xu Guo, Wen Wang, Jiamin Ji, Tianchen Wei, Tao Ouyang

School of Materials Science and Engineering, Shaanxi Key Laboratory of Green Preparation and Functionalization for Inorganic Materials, Shaanxi University of Science & Technology, Xi'an, 710021, People's Republic of China

ARTICLE INFO

Keywords:
High entropy ceramics
Phase stability
Grain growth
Dielectric properties

ABSTRACT

A series of high entropy Ba($Zr_{0.2}Ti_{0.2}Sn_{0.2}Hf_{0.2}Me_{0.2}$)$O_3$ (Me = Y^{3+},Nb^{5+},Ta^{5+},V^{5+},Mo^{6+},W^{6+}) perovskite oxides were synthesized by using a solid state reaction method. Three multiple-cation solid solutions formed pure phase compounds, and only two compounds were sintered into ceramics. Microstructure analysis showed the influence of configurational entropy on phase stability and grain growth. Dielectric measurements showed that the high entropy ceramics possessed decent temperature stability of permittivity from 25 °C to 200 °C, low dielectric loss (< 0.002) from 20 Hz to 2 MHz, high resistance and moderate breakdown strength (290 kV/cm, 370 kV/cm). Evidence strongly confirmed that controlling configurational entropy could be a feasible perspective to set up highly tunable perovskite structures and explore novel species of dielectric materials.

1. Introduction

Over the past dozen years, high entropy alloys (HEAs) have drawn particular attention on account of the pursuit for high mechanical strength, ductility, hardness and better wear/corrosion resistance than conventional alloys [1–6]. It was found that HEAs possessing unique and stable structures can be intentionally designed through the control of configurational entropy, which is defined as followed equation: $\Delta S_{config} = -R\sum_{i=1}^{n} x_i \ln x_i$. R is gas constant and x_i is the molar content of the *i*th element. Apparently, multiplying component and adjusting the relative ratio between each element leads to an increase of ΔS_{config}. Thus, from a perspective of thermodynamics, the materials are classified into "low entropy" ($S_{config} < 1$ R), "medium entropy" (1 R ≤ $S_{config} < 1.5$ R) and "high entropy" ($S_{config} > 1.5$ R) systems [7]. Recently, Lei et al. present the concept "entropy engineering" which means designing materials through the control of configurational entropy [8].

Inspired by the studies of HEAs, Tsau et al. fabricated a series of high entropy and medium entropy alloy oxides, which meant an significant expansion of concept from HEAs to more other classes of high entropy materials [9]. From then onwards, there has been an upsurge in the investigation of high entropy oxides (HEOs) [10–29], high entropy carbides (HECs) [30–32], high entropy nitrides (HENs) [33–35], high entropy borides (HEBs) [36,37], and high entropy silicide (HESs) [38]. Then, under the guidance of this new approach (i.e., multiplying five/more than five elements into cation sublattice), some attractive properties were developed in the realm of reversible energy storage [11,25], CO oxidation catalysts [12], magnetic properties [14,19], and mechanical properties [16,30–32]. However, a majority of these research are regarding rock-salt structures. Investigation of other crystal structures remain to be further explored since the "high entropy" has been induced to many kinds of crystal structures. Perovskite type oxides (ABO_3) have more complex structures than rock-salt type oxides and they are more flexible to form high entropy compounds due to the two cationic sublattice sites (*A*-site and *B*-site). Therefore, it will be more convincing to confirm the effect of S_{config} in such complex structures, so that S_{config} can be better correlated with the properties.

In this present paper, we report six types of perovskite-based high entropy oxides (PE-HEOs) Ba($Zr_{0.2}Ti_{0.2}Sn_{0.2}Hf_{0.2}Me_{0.2}$)$O_3$ (Me = Y^{3+},Nb^{5+},Ta^{5+},V^{5+},Mo^{6+},W^{6+}). Among them, the Ba($Zr_{0.2}Ti_{0.2}Sn_{0.2}Hf_{0.2}Me_{0.2}$)$O_3$ (Me = Nb^{5+},Ta^{5+}) powders were sintered into ceramics. The role of S_{config} in phase stabilization was investigated by creating nine quaternary medium entropy systems. Especially, according to the measurement results, we bridged the relationship between dielectric properties and high S_{config} structures from many perspectives and proposed methods for further tailoring properties of the high entropy parent materials.

* Corresponding author.
E-mail address: labelectroceramic@sust.edu.cn (Y. Pu).

https://doi.org/10.1016/j.ceramint.2019.11.239
Received 5 November 2019; Received in revised form 19 November 2019; Accepted 26 November 2019
Available online 27 November 2019

2. Experimental procedure

$Ba(Zr_{0.2}Ti_{0.2}Sn_{0.2}Hf_{0.2}Me_{0.2})O_3$ ($Me = Y^{3+}, Nb^{5+}, Ta^{5+}, V^{5+}, Mo^{6+}, W^{6+}$) powders were synthesized by using conventional solid-state reaction method. Analytically pure reagents $BaCO_3$, ZrO_2, TiO_2, SnO_2, HfO_2, Y_2O_3, Nb_2O_5, Ta_2O_5, V_2O_5, MoO_3, WO_3 were selected as the raw materials, weighted in stoichiometric ratios and milled in the PTFE jars with deionized water as the medium. For the sake of the formation of uniform mixture, the powders were grinded for 8 h, after which the dried mixture were calcined from 1250 °C to 1350 °C for 10 h to ensure that all the complex components reacted completely. $Ba(Zr_{0.2}Ti_{0.2}Sn_{0.2}Hf_{0.2}Me_{0.2})O_3$ ($Me = Y^{3+}, Nb^{5+}, Ta^{5+}$) powders were then milled twice and pressed into the shape of discs which were 10 mm in diameter and 1.2 mm in thickness using cold isostatical method. Subsequently all the pellets were sintered in air for 2 h at a temperature range of 1480–1630 °C.

The Archimedean drainage method was utilized to measure the density of the ceramics. X-ray diffraction (XRD, D/max-2200PC, RIGAKU, Japan) was detected to analyze the phase composition. Microstructure of two samples were observed by field emission scanning electron microscope (FE-SEM, S-4800, RIGAKU Co, Japan) equipped with energy-dispersive spectrometer (EDS) for elemental composition analysis. Before the electrical performance measurements, the samples should be coated by a silver paste to form an electron. The dielectric properties were tested via impedance analyzer (Agilent E4980A, USA). The polarization-electric field (*P-E*) hysteresis loops were obtained from a ferroelectric analyzer (Premier II, Radiant, USA).

3. Results and discussion

Fig. 1(a) are the XRD patterns of the $Ba(Zr_{0.2}Ti_{0.2}Sn_{0.2}Hf_{0.2}Me_{0.2})O_3$ ($Me = Y^{3+}, Nb^{5+}, Ta^{5+}, V^{5+}, Mo^{6+}, W^{6+}$) powders calcined at 1350 °C. During the experiments, the powders ($Me = Y^{3+}, Nb^{5+}, Ta^{5+}$) gradually form the single-phase solid solutions with the increase of temperature, while the powders ($Me = V^{5+}, Mo^{6+}, W^{6+}$) fail to become single-phase and some second phase emerge. For HEAs, the average atomic-size difference (δ) which originates from Hume-Rothery solid-solution rule is calculated by the equation:

$$\delta = \sqrt{\sum_{i=1}^{N} x_i \left[1 - R_i / \left(\sum_{i=1}^{N} x_i R_i\right)\right]^2} \quad (1)$$

where R_i is the ith element's ionic radius and x_i is its mole fraction [38].

Table 1
Oxidation state, co-ordination number (CN) and corresponding cationic radii (r_c).

Element	Oxidation	CN	r_c [Å]
Ba	+2	XII	1.61
Zr	+4	VI	0.72
Ti	+4	VI	0.61
Sn	+4	VI	0.69
Hf	+4	VI	0.71
Y	+3	VI	0.90
Nb	+5	VI	0.64
Ta	+5	VI	0.64
V	+5	VI	0.54
Mo	+6	VI	0.59
W	+6	VI	0.60

When $\delta \leq 4\%$, the HEAs become single-phase HEAs [39]. However, for perovskite oxides, previous reports suggested that the Goldschmidt tolerance factor (t) is more reliable to determine a single-phase structure and defined as follow:

$$t = \frac{R_A + R_O}{\sqrt{2}(R_B + R_O)} \quad (2)$$

where R_A, R_B and R_O are ionic radii of A, B and oxygen site in perovskite oxides [17]. When A/B site is occupied by multiple ions, $\bar{R}_A/\bar{R}_B$ is the proper value to calculate. Fig. 1(b) shows the tolerance factors (t) and the lattice parameters (a) of the six powders. Evidently, tolerance factor is monotone increase. For the components when $Me = Mo^{6+}, W^{6+}, V^{5+}$, the tolerance factors of these powders are above 1.03 and second phases only exist in these three components as well. This result is consistent with prior reports by Jiang et al. as well [17]. In addition, compared with the $Ba(Zr_{0.2}Ti_{0.2}Sn_{0.2}Hf_{0.2}Me_{0.2})O_3$ ($Me = Y^{3+}, Nb^{5+}, Ta^{5+}$) powders, lattice parameters of the Ba $(Zr_{0.2}Ti_{0.2}Sn_{0.2}Hf_{0.2}Me_{0.2})O_3$ ($Me = Mo^{6+}, W^{6+}, V^{5+}$) increase due to the existence of second phase. Oxidation state, co-ordination number (CN) and corresponding cationic radii (r_c) of each element are listed in Table 1.

During the sintering experiments of the three pure-phase PE-HEOs, the component $Ba(Zr_{0.2}Ti_{0.2}Sn_{0.2}Hf_{0.2}Y_{0.2})O_3$ cannot become ceramics even at 1630 °C, which is beyond the expectation. For this component, electric current assisted sintering methods like SPS (spark plasma sintering) and FS (flash sintering) should probably be considered for the further studies since these two methods were proved to successfully

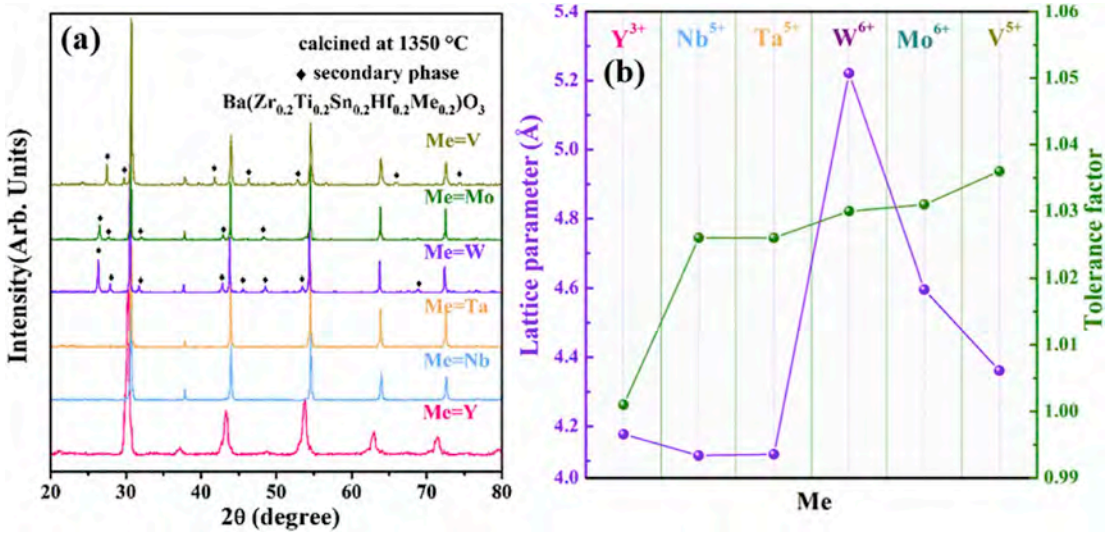

Fig. 1. (a) XRD pattern of $Ba(Zr_{0.2}Ti_{0.2}Sn_{0.2}Hf_{0.2}Me_{0.2})O_3$ ($Me = Y^{3+}, Nb^{5+}, Ta^{5+}, V^{5+}, Mo^{6+}, W^{6+}$) powders calcined at 1350 °C (b) tolerance factors and lattice parameters of $Ba(Zr_{0.2}Ti_{0.2}Sn_{0.2}Hf_{0.2}Me_{0.2})O_3$ ($Me = Y^{3+}, Nb^{5+}, Ta^{5+}, V^{5+}, Mo^{6+}, W^{6+}$) powders calcined at 1350 °C.

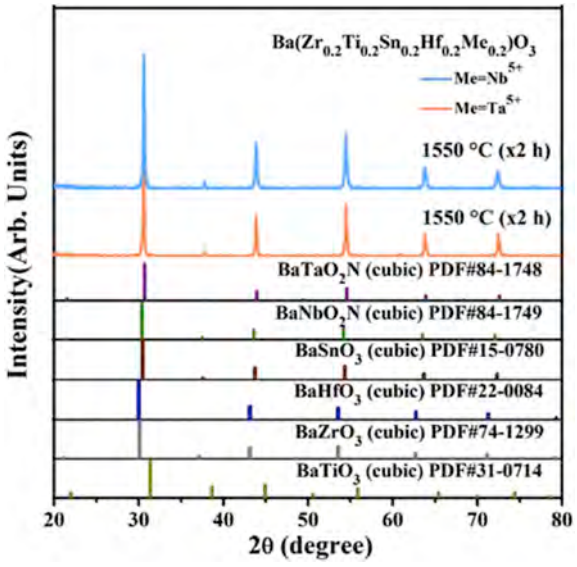

Fig. 2. XRD patterns of $Ba(Zr_{0.2}Ti_{0.2}Sn_{0.2}Hf_{0.2}Me_{0.2})O_3$ ($Me = Nb^{5+}$, Ta^{5+}) ceramics sintered at 1550 °C.

sinter some kinds of perovskite oxides which are hard to form dense ceramics [23,40]. Fig. 2 shows the XRD patterns of $Ba(Zr_{0.2}Ti_{0.2}Sn_{0.2}Hf_{0.2}Me_{0.2})O_3$ ($Me = Nb^{5+}$,Ta^{5+}) ceramics sintered at 1550 °C. PDF standard cards below the patterns indicate that the two ceramics form pure pseudo cubic phase without any second phase, considering that the complex lattice distortion is created by multiple ions in *B*-site and the Goldschmidt tolerance factors of the two ceramics (1.03) are above 1 (the value of ideal cubic perovskite crystal). Among these PDF cards, the one of $BaSnO_3$ matches best because the radius of tin ion (0.64 Å) is closest to the average radius in B-site (0.674 Å). SEM micrographs of the $Ba(Zr_{0.2}Ti_{0.2}Sn_{0.2}Hf_{0.2}Me_{0.2})O_3$ ($Me = Nb^{5+}$,Ta^{5+}) ceramics are displayed in Fig. 3 (a) and (b). The grain boundary of the both samples can be observed clearly and pores are almost invisible throughout the samples, which correspond to the results of density calculation (i.e. the relative density of the ceramics reaches 92% and 95%, respectively). Meanwhile, the small grain size illustrate that the extremely disordered grain interior created by mixing five cations in *B*-site restrain the grain growth. To further verify the homogeneity of element distribution, EDS mappings of the two ceramic samples are shown in Fig. 3 (c) and (d). For each ceramic sample, all the five elements uniformly distribute in the same region without any segregation or aggregation of the elements.

In order to further investigate the influence of configurational entropy on system stability, nine quaternary powders are calcined at the same temperature at which $Ba(Zr_{0.2}Ti_{0.2}Sn_{0.2}Hf_{0.2}Me_{0.2})O_3$ ($Me = Nb^{5+}$,Ta^{5+}) powders become the single phase compounds. As shown in Fig. 4, all the samples form the second phase, which just varies in the amount. For the generated second phase, t and δ_B of these quaternary systems are calculated at first. However, all the values of δ_B are small and some tolerance factors of the systems are less than 1.03, which is the critical value for forming a single phase in the high entropy system mentioned above. As the number of elements decrease, the S_{config} goes down to 1.39 R. At the same calcining temperature, medium entropy systems fail to compensate for the high enthalpy which is the driving force for phase separation [18]. These results confirm that high configurational entropy plays a major role in stabilizing the single phase structure of the complex multicomponent perovskite oxides. The tolerance factors (t), lattice parameters(a), the average atomic-size difference in B-site (δ_B), and the presence of a second phase in the high entropy systems and medium entropy systems are listed in Table 2.

The permittivity and dielectric loss as functions of frequency and temperature of $Ba(Zr_{0.2}Ti_{0.2}Sn_{0.2}Hf_{0.2}Me_{0.2})O_3$ ($Me = Nb^{5+}$,Ta^{5+}) ceramics are presented in Fig. 5. It is clearly to see that the permittivity possesses excellent stability at a wide temperature window and loss tangent is quite low (< 0.002) in a frequency range of 20 Hz-2 MHz. In light of the former investigation on how configurational entropy affect thermal and electrochemical stability, it can be deduced that entropy stability also contributes to the stability of permittivity and loss tangent since the change of these two parameter can attribute to the phase transformation and structural stability [11,41]. The relatively low permittivity of the two ceramic samples is associated with the minor concentration of titanium content in *B*-site and the small grain size. Meanwhile, this result also manifests that *B*-site sublattice has a large impact on dielectric properties and carries transport properties for perovskite oxides [20].

The complex impedance spectrums of $Ba(Zr_{0.2}Ti_{0.2}Sn_{0.2}Hf_{0.2}Me_{0.2})O_3$ ($Me = Nb^{5+}$,Ta^{5+}) ceramics are shown in Fig. 6. When $Me = Ta^{5+}$, there are two distinct semicircles in the spectrum which are simulated

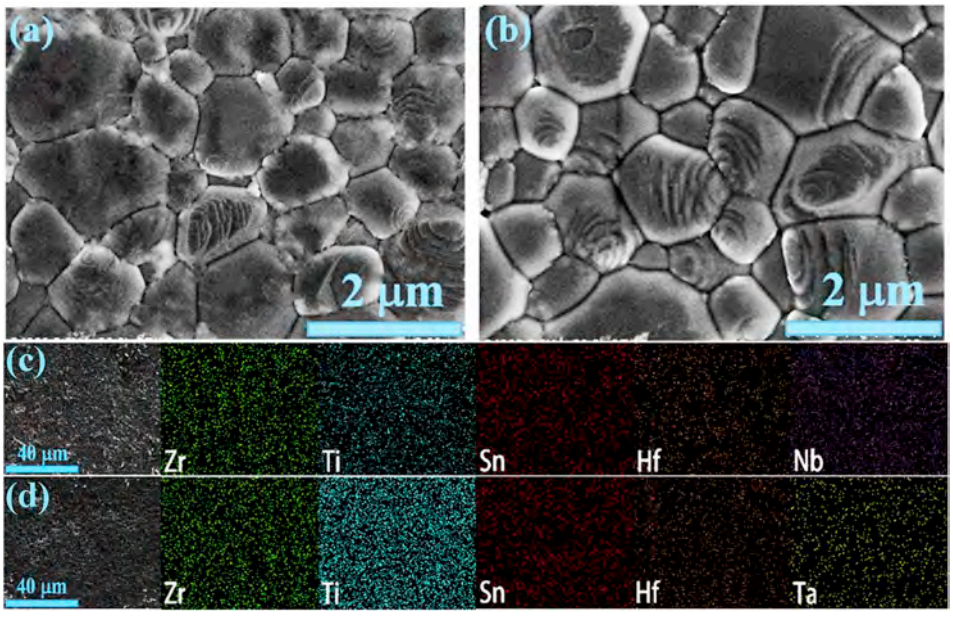

Fig. 3. Cross sectional SEM micrographs and related EDS elemental maps for $Ba(Zr_{0.2}Ti_{0.2}Sn_{0.2}Hf_{0.2}Me_{0.2})O_3$ ceramic samples: (a, c) $Me = Nb^{5+}$, (b, d) $Me = Ta^{5+}$.

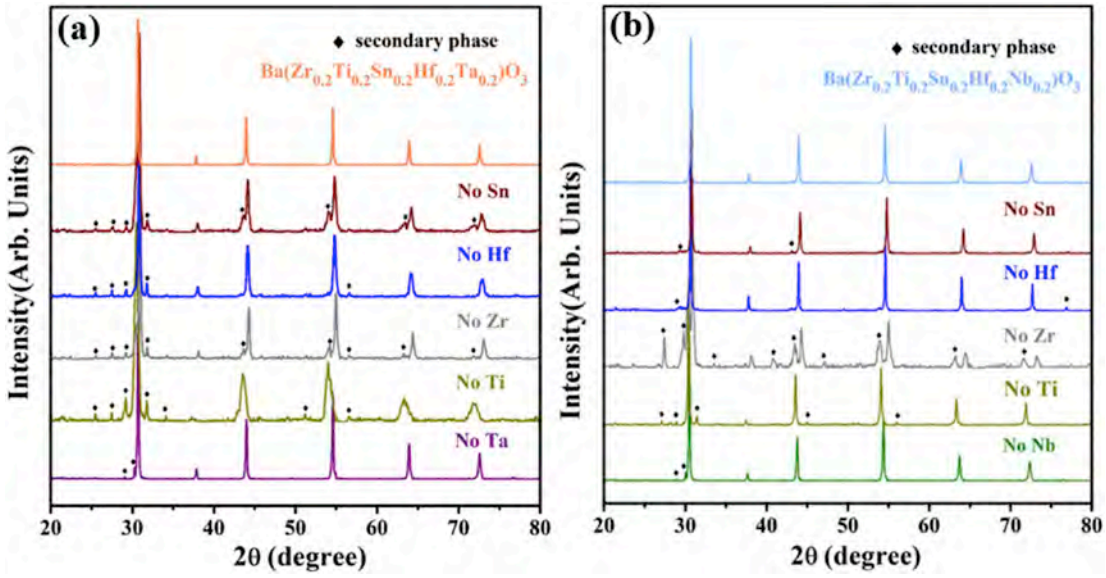

Fig. 4. XRD patterns of the quaternary systems where individual components are removed from the $Ba(Zr_{0.2}Ti_{0.2}Sn_{0.2}Hf_{0.2}Me_{0.2})O_3$ powders calcined at 1350 °C: (a) $Me = Ta^{5+}$, (b) $Me = Nb^{5+}$.

Table 2
The tolerance factors (*t*), lattice parameters(*a*), the average atomic-size difference in B-site (δ_B), and the presence of a second phase in the components.

	Second phase?	*t*	*a*	δ_B
$Ba(Zr_{0.2}Ti_{0.2}Sn_{0.2}Hf_{0.2}Y_{0.2})O_3$	No	1.001	4.177	13.4%
$Ba(Zr_{0.2}Ti_{0.2}Sn_{0.2}Hf_{0.2}Nb_{0.2})O_3$	No	1.026	4.115	6%
$Ba(Zr_{0.2}Ti_{0.2}Sn_{0.2}Hf_{0.2}Ta_{0.2})O_3$	No	1.026	4.119	6%
$Ba(Zr_{0.2}Ti_{0.2}Sn_{0.2}Hf_{0.2}W_{0.2})O_3$	Yes	1.03	5.221	7.6%
$Ba(Zr_{0.2}Ti_{0.2}Sn_{0.2}Hf_{0.2}Mo_{0.2})O_3$	Yes	1.031	4.596	8.1%
$Ba(Zr_{0.2}Ti_{0.2}Sn_{0.2}Hf_{0.2}V_{0.2})O_3$	Yes	1.036	4.361	10.5%
$Ba(Zr_{0.25}Ti_{0.25}Sn_{0.25}Nb_{0.25})O_3$	Yes	1.031	4.102	6%
$Ba(Zr_{0.25}Ti_{0.25}Hf_{0.25}Nb_{0.25})O_3$	Yes	1.028	4.181	6.9%
$Ba(Ti_{0.25}Sn_{0.25}Hf_{0.25}Nb_{0.25})O_3$	Yes	1.032	4.099	5.98%
$Ba(Zr_{0.2}5Sn_{0.25}Hf_{0.25}Nb_{0.25})O_3$	Yes	1.019	4.396	4.47%
$Ba(Zr_{0.25}Ti_{0.25}Sn_{0.25}Ta_{0.25})O_3$	Yes	1.031	4.079	6%
$Ba(Zr_{0.25}Ti_{0.25}Hf_{0.25}Ta_{0.25})O_3$	Yes	1.028	4.2503	6.9%
$Ba(Ti_{0.25}Sn_{0.25}Hf_{0.25}Ta_{0.25})O_3$	Yes	1.032	4.105	5.98%
$Ba(Zr_{0.2}5Sn_{0.25}Hf_{0.25}Ta_{0.25})O_3$	Yes	1.019	4.162	4.47%
$Ba(Zr_{0.25}Ti_{0.25}Sn_{0.25}Hf_{0.25})O_3$	Yes	1.022	4.12	6%

utilizing an equivalent circuit with two parallel *R-C* in series. Apparently, the semicircle in high frequency is larger than that in low frequency which confirms that grain boundary resistance (R_{gb}) is lower than grain resistance (R_g). This is due to the sever lattice distortion and strongly disordered grain interiors caused by a complex random arrangement of multiple cations [42]. Therefore, the role of grain in suppressing the long-range motion of electron is amplified. Yet when $Me = Nb^{5+}$, only one semicircle exists in the spectrum which is due to the close resistance value between grain and grain boundary.

Fig. 7(a) and (b) exhibits the frequency dependence of conductivity for the two ceramic samples. Extremely low conductivity can be observed from both of the figures which illustrate the role of high mixing entropy in improving insulation performance (i.e., impeding the hopping of charge carriers) as well. A flat platform before approaching 10^5 Hz denotes that the conductivity approximates dc values [43]. To obtain the activation energy of grain (E_g) and grain boundary (E_{gb}), Arrhenius equation is adopted as below:

$$\sigma = \sigma_0 \exp\left(-\frac{E_a}{K_B T}\right) \tag{3}$$

where Boltzmann constant (k_B) and pre-exponential term (σ_0) are two constant parameters. As shown in Fig. 7(c) and (d), when $Me = Ta^{5+}$, the activation energy of grain (E_g) and grain boundary (E_{gb}) are 0.59 eV and 0.68 eV, and when $Me = Nb^{5+}$, the E_g and E_{gb} are 0.68 eV and 0.70 eV, respectively. Distinct difference between the E_g and E_{gb} in both ceramic samples demonstrates that electrons are not able to cluster at the grain boundary, which benefits to reduce the space charge polarization and the dielectric loss (tanδ) of both ceramic samples [43].

Fig. 8 is the unipolar *P-E* loops measured at 10 Hz of the two ceramics. As it shows, the plots are in the slim shapes possessing small remnant polarization (P_r). With the increase of electric field, the shape of the *P-E* loops change slightly which can be ascribed to a large mixture of nonferroelectric elements and the low energy loss. It is noteworthy that breakdown electric field (E_b) of Ba $(Zr_{0.2}Ti_{0.2}Sn_{0.2}Hf_{0.2}Me_{0.2})O_3$ ($Me = Nb^{5+}, Ta^{5+}$) ceramics reach 290 kV/cm and 370 kV/cm, respectively. On one hand, high configurational entropy forms a extremely disordered grain interior, restricts the hooping of carriers in a long range and leads to a high resistance which benefis for improving E_b [8,44,45]. On the other hand, this kind of disorder reduces the driving force of grain growth. In terms of the direct relation between $E_b \propto 1/G^{-1/2}$ where G is the grain size, small size of grain bulk also benefits for a high E_b [46]. Meanwhile, in accordance to the equation for discharge energy storage density (W_D):

$$W_D = \int_{P_r}^{P_s} EdP \tag{4}$$

where P_s, P_r, E denote saturated polarization, remnent polarization, and electric field, respectively, high breakdown strength is beneficial to excellent energy storage properties. Indeed, the calculation results show that the discharge energy storage density of the Ba $(Zr_{0.2}Ti_{0.2}Sn_{0.2}Hf_{0.2}Me_{0.2})O_3$ ceramics (0.55 J/cm^3 when $Me = Nb^{5+}$, 0.68 J/cm^3 when $Me = Ta^{5+}$) is higher than many lead-free parent dielectric materials such as $BaTiO_3$ (0.08 J/cm^3), $Ba_{0.65}Sr_{0.35}TiO_3$ (0.28 J/cm^3), $BaZr_{0.1}Ti_{0.9}O_3$ (0.5 J/cm^3), $BaTi_{0.85}Sn_{0.15}O_3$ (0.35 J/cm^3), $Ba_{0.9}Sr_{0.1}Zr_{0.2}Ti_{0.8}O_3$ (0.42 J/cm^3) [47–51]. In designing our high entropy ceramics for energy storage application, further studies should focus on improving the permittivity and saturated polarization by changing the relative proportion of each ions or doping other cations in the parent high entropy materials like Bi and Sr in *A*-site [52–54].

4. Conclusion

This work verified that the formation of pure-phase PE-HEOs can be

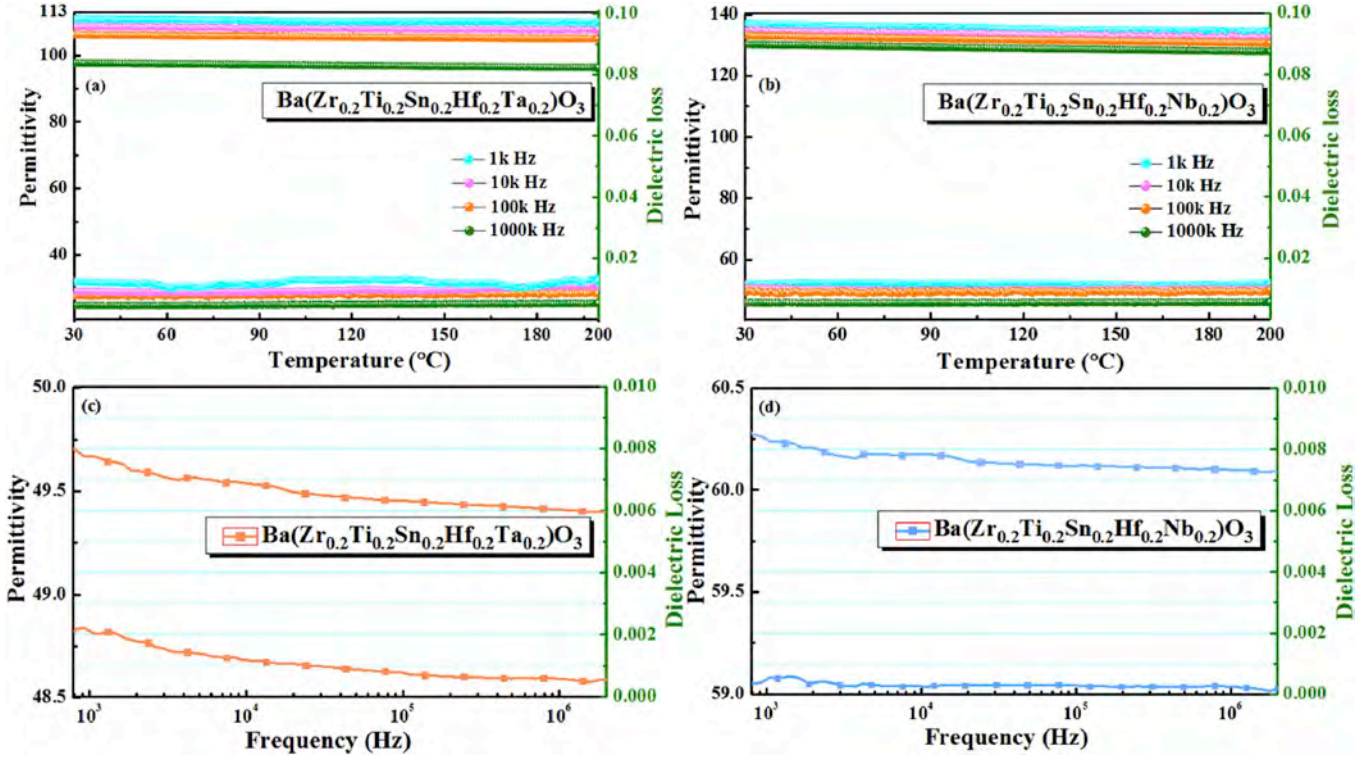

Fig. 5. Temperature and frequency dependence of permittivity and dielectric loss of $Ba(Zr_{0.2}Ti_{0.2}Sn_{0.2}Hf_{0.2}Me_{0.2})O_3$ ceramics: (a, c) Me = Ta^{5+}, (b, d) Me = Nb^{5+}.

preliminarily determined by the calculation of tolerance factor. Cation-removement experiment showed the existance of the second phase in the medium entropy powders calcined at the same temperature as the high entropy powders. Thus, the unique role of high configurational entropy in stabilizing the single phase structure of complex perovskite systems was confirmed. In addition, due to the high configurational entropy, the $Ba(Zr_{0.2}Ti_{0.2}Sn_{0.2}Hf_{0.2}Me_{0.2})O_3$ ceramics possessed some peculiar dielectric properties such as excellent temperature stability of permittivity from 25 °C to 200 °C, low dielectric loss (< 0.002) from 20 Hz to 2 MHz, large resistance and moderate breakdown strength (290 kV/cm and 370 kV/cm). For PE-HEOs, highly disordered grain interior, severe lattice distortion and slow diffusion effect inside the grain are the most typical characteristics and the springboard to develop the application areas of them. On the basis of the entropy engineering and the definition of high entropy (S_{config} > 1.5 R), adjusting the ratio between ions and doping one or several elements in the parent materials can be further considered to improve dielectric properties. We hold the view that entropy engineering will be a brand new approach to design and enrich dielectric materials.

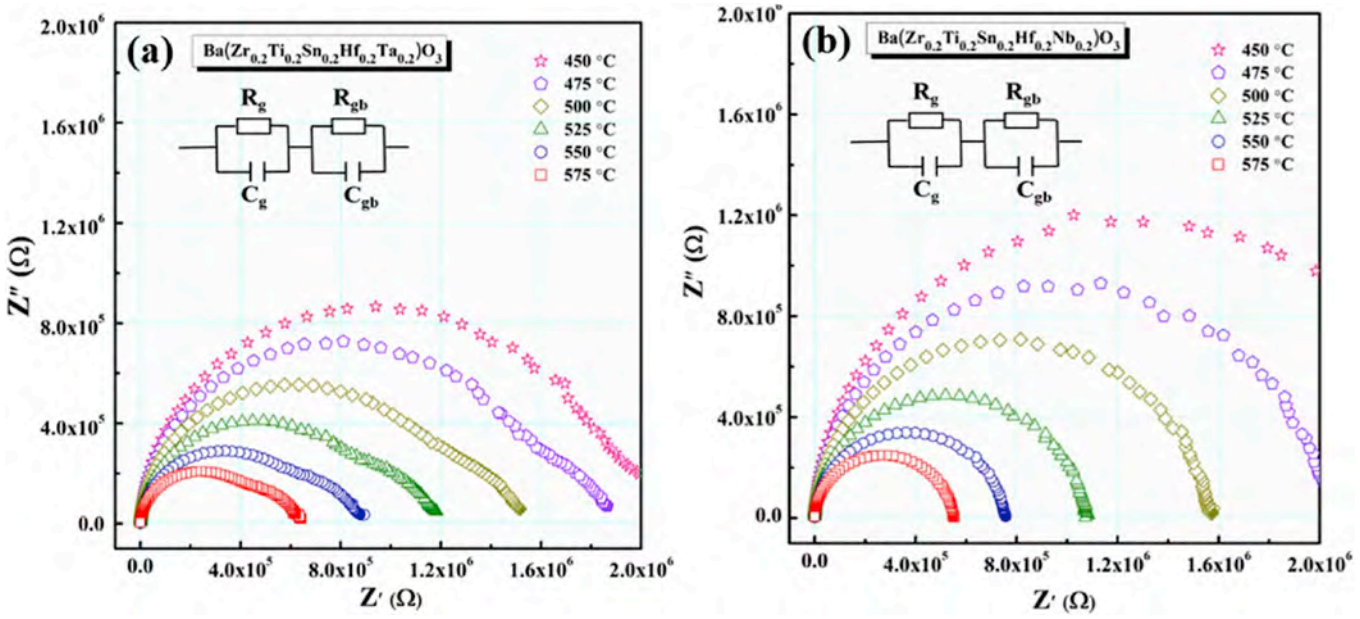

Fig. 6. Complex impedance spectrums of $Ba(Zr_{0.2}Ti_{0.2}Sn_{0.2}Hf_{0.2}Me_{0.2})O_3$ ceramics, (a)Me = Ta^{5+}, (b) Me = Nb^{5+}.

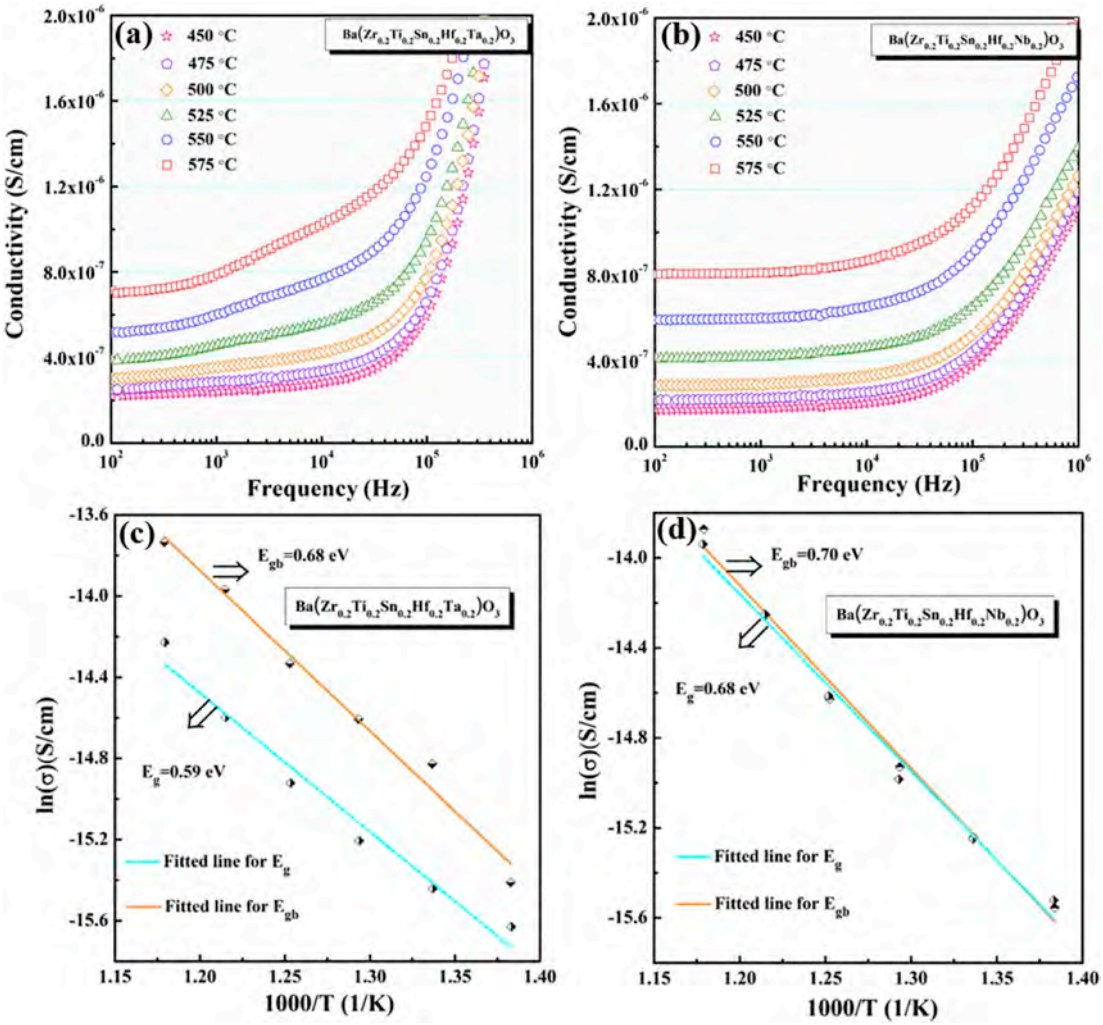

Fig. 7. Frequency dependence of conductivity (450–575 °C) and Arrhenius plots of ln(*f*) vs. 1000/T of $Ba(Zr_{0.2}Ti_{0.2}Sn_{0.2}Hf_{0.2}Me_{0.2})O_3$ ceramics, (a, c) Me = Ta^{5+}, (b, d)Me = Nb^{5+}.

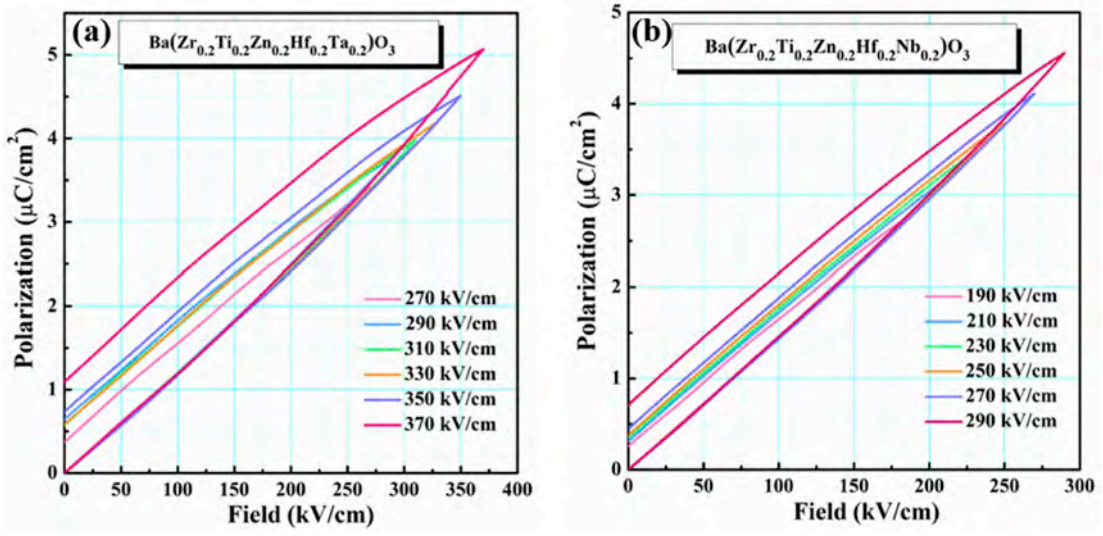

Fig. 8. Unipolar *P-E* loops measured at 10 Hz under critical electric field of $Ba(Zr_{0.2}Ti_{0.2}Sn_{0.2}Hf_{0.2}Me_{0.2})O_3$ ceramics, (a)Me = Ta^{5+}, (b) Me = Nb^{5+}.

Declaration of competing interest

The authors declare that they have no known competing financial interests or personal relationships that could have appeared to influence the work reported in this paper.

Acknowledgements

The authors are grateful for the financial support from the National Natural Science Foundation of China (51872175), the International Cooperation Projects of Shaanxi Province (2018KW-027).

References

[1] J.W. Yeh, S.-K. Chen, S.-J. Lin, J.-Y. Gan, T.-S. Chin, T.-T. Shun, C.-H. Tsau, S.-Y. Chang, Nanostructured high-entropy alloys with multiple principal elements: novel alloy design concepts and outcomes, Adv. Eng. Mater. 6 (2004) 299–303, https://doi.org/10.1002/adem.200300567.

[2] J. Li, W. Jia, J. Wang, H. Kou, D. Zhang, E. Beaugnon, Enhanced mechanical properties of a CoCrFeNi high entropy alloy by supercooling method, Mater. Des. 95 (2016) 183–187, https://doi.org/10.1016/j.matdes.2016.01.112.

[3] X. Xian, Z. Zhong, B. Zhang, K. Song, C. Chen, S. Wang, J. Cheng, Y. Wu, A high-entropy $V_{35}Ti_{35}Fe_{15}Cr_{10}Zr_5$ alloy with excellent high-temperature strength, Mater. Des. 121 (2017) 229–236, https://doi.org/10.1016/j.matdes.2017.02.029.

[4] M.C. Gao, D.B. Miracle, D. Maurice, X. Yan, Y. Zhang, J.A. Hawk, High-entropy functional materials, J. Mater. Res. 33 (2018) 3138–3155, https://doi.org/10.1557/jmr.2018.32.

[5] D.B. Miracle, O.N. Senkov, A critical review of high entropy alloys and related concepts, Acta Mater. 122 (2017) 448–511, https://doi.org/10.1016/j.actamat.2016.08.081.

[6] W. Huo, H. Zhou, F. Fang, Z. Xie, J. Jiang, Microstructure and mechanical properties of CoCrFeNiZr$_x$ eutectic high-entropy alloys, Mater. Des. 134 (2017) 226–233, https://doi.org/10.1016/j.matdes.2017.08.030.

[7] B.S. Murty, J.W. Yeh, S. Ranganathan, High-Entropy Alloys, Butterworth-Heinemann, London, 2014, https://doi.org/10.1016/B978-0-12-800251-3.00010-9.

[8] Z. Lei, X. Liu, H. Wang, Y. Wu, S. Jiang, Z. Lu, Development of advanced materials via entropy engineering, Scr. Mater. 165 (2019) 164–169, https://doi.org/10.1016/j.scriptamat.2019.02.015.

[9] C. Tsau, Y. Yang, C. Lee, L. Wu, H. Huang, The low electrical resistivity of the high-entropy alloy oxide thin films, Procedia Eng. 36 (2012) 246–252, https://doi.org/10.1016/j.proeng.2012.03.037.

[10] C.M. Rost, E. Sachet, T. Borman, A. Moballegh, E.C. Dickey, D. Hou, J.L. Jones, S. Curtarolo, J.-P. Maria, Entropy-stabilised oxides, Nat. Commun. 6 (2015) 8485, https://doi.org/10.1038/ncomms9485.

[11] A. Sarkar, L. Velasco, D. Wang, Q. Wang, G. Talasila, L. de Biasi, C. Kubel, T. Brezesinski, S.S. Bhattacharya, H. Hahn, B. Breitung, High entropy oxides for reversible energy storage, Nat. Commun. 9 (2018) 3400, https://doi.org/10.1038/s41467-018-05774-5.

[12] D. Bérardan, S. Franger, D. Dragoe, A.K. Meena, N. Dragoe, Colossal dielectric constant in high entropy oxides, Phys. Status Solidi Rapid Res. Lett. 10 (2016) 328–333, https://doi.org/10.1002/pssr.201600043.

[13] H. Chen, J. Fu, P. Zhang, H. Peng, C.W. Abney, K. Jie, X. Liu, M. Chi, S. Dai, Entropy-stabilized metal oxide solid solutions as CO oxidation catalysts with high-temperature stability, J. Mater. Chem. A. tr6 (2018) 11129–11133, https://doi.org/10.1039/C8TA01772G.

[14] P.B. Meisenheimer, T.J. Kratofil, J.T. Heron, Giant enhancement of exchange coupling in entropy-stabilized oxide heterostructures, Sci. Rep. 7 (2017) 13344, https://doi.org/10.1038/s41598-017-13810-5.

[15] A. Sarkar, C. Loho, L. Velasco, T. Thomas, S.S. Bhattacharya, H. Hahn, R. Djenadic, Multicomponent equiatomic rare earth oxides with a narrow band gap and associated praseodymium multivalency, Dalton Trans. 46 (2017) 12167–12176, https://doi.org/10.1039/C7DT02077E.

[16] J. Gild, M. Samiee, J.L. Braun, T. Harrington, H. Vega, P.E. Hopkins, K. Vecchio, J. Luo, High-entropy fluorite oxides, J. Eur. Ceram. Soc. 38 (2018) 3578–3584, https://doi.org/10.1016/j.jeurceramsoc.2018.04.01.

[17] S. Jiang, T. Hu, J. Gild, N. Zhou, J. Nie, M. Qin, T. Harrington, K. Vecchio, J. Luo, A new class of high-entropy perovskite oxides, Scr. Mater. 142 (2018) 116–120, https://doi.org/10.1016/j.scriptamat.2017.08.040.

[18] A. Sarkar, R. Djenadic, D. Wang, C. Hein, R. Kautenburger, O. Clemens, H. Hahn, Rare earth and transition metal based entropy stabilised perovskite type oxides, J. Eur. Ceram. Soc. 38 (2018) 2318–2327, https://doi.org/10.1016/j.jeurceramsoc.2017.12.058.

[19] R. Witte, A. Sarkar, R. Kruk, B. Eggert, R.A. Brand, H. Wende, H. Hahn, High entropy oxides: an emerging prospect for magnetic rare earth - transition metal perovskites, Phys. Rev. Mater. 3 (2019) 034406, https://doi.org/10.1103/PhysRevMaterials.3.034406.

[20] Y. Sharma, B.L. Musico, X. Gao, C. Hua, A.F. May, A. Herklotz, A. Rastogi, D. Mandrus, J. Yan, H.N. Lee, M.F. Chisholm, V. Keppens, T.Z. Ward, Single-crystal high entropy perovskite oxide epitaxial films, Phys. Rev. Mater. 2 (2018), https://doi.org/10.1103/PhysRevMaterials.2.060404.

[21] M.R. Chellali, A. Sarkar, S.H. Nandam, S.S. Bhattacharya, B. Breitung, H. Hahn, L. Velasco, On the homogeneity of high entropy oxides: an investigation at the atomic scale, Scr. Mater. 166 (2019) 58–63, https://doi.org/10.1016/j.scriptamat.2019.02.039.

[22] Y. Zhong, H. Sabarou, X. Yan, M. Yang, M.C. Gao, X. Liu, R.D. Sisson, Exploration of high entropy ceramics (HECs) with computational thermodynamics - a case study with $LaMnO_{3\pm\delta}$, Mater. Des. 182 (2019) 108060, https://doi.org/10.1016/j.matdes.2019.108060.

[23] M. Biesuz, S. Fu, J. Dong, A. Jiang, D. Ke, Q. Xu, D. Zhu, M. Bortolotti, M.J. Reece, C. Hu, S. Grasso, High entropy $Sr((Zr_{0.94}Y_{0.06})_{0.2}Sn_{0.2}Ti_{0.2}Hf_{0.2}Mn_{0.2})O_{3-x}$ perovskite synthesis by reactive spark plasma sintering, J. As. Ceram. Soc. 7 (2019) 127–132, https://doi.org/10.1080/21870764.2019.1595931.

[24] J. Dąbrowa, M. Stygar, A. Mikuła, A. Knapik, K. Mroczka, W. Tejchman, M. Danielewski, M. Martin, Synthesis and microstructure of the $(Co,Cr,Fe,Mn,Ni)_3O_4$ high entropy oxide characterized by spinel structure, Mater. Lett. 216 (2018) 32–36, https://doi.org/10.1016/j.matlet.2017.12.148.

[25] A. Sarkar, Q. Wang, A. Schiele, M.R. Chellali, S.S. Bhattacharya, D. Wang, T. Brezesinski, H. Hahn, L. Velasco, B. Breitung, High-entropy oxides: fundamental aspects and electrochemical properties, Adv. Mater. 31 (2019) e1806236, , https://doi.org/10.1002/adma.201806236.

[26] G. Anand, A.P. Wynn, C.M. Handley, C.L. Freeman, Phase stability and distortion in high-entropy oxides, Acta Mater. 146 (2018) 119–125, https://doi.org/10.1016/j.actamat.2017.12.037.

[27] C.M. Rost, Z. Rak, D.W. Brenner, J. Maria, Local structure of the $Mg_xNi_xCo_xCu_xZn_xO$ (x = 0.2) entropy-stabilized oxide: an EXAFS study, J. Am. Ceram. Soc. 100 (2017) 2732–2738, https://doi.org/10.1111/jace.14756.

[28] Z. Grzesik, G. Smoła, M. Stygar, J. Dąbrowa, M. Zajusz, K. Mroczka, M. Danielewski, Defect structure and transport properties in (Co,Cu,Mg,Ni,Zn)O high entropy oxide, J. Eur. Ceram. Soc. 39 (2019) 4292–4298, https://doi.org/10.1016/j.jeurceramsoc.2019.06.018.

[29] K. Chen, X. Pei, L. Tang, H. Cheng, Z. Li, C. Li, X. Zhang, L. An, A five-component entropy-stabilized fluorite oxide, J. Eur. Ceram. Soc. 38 (2018) 4161–4164, https://doi.org/10.1016/j.jeurceramsoc.2018.04.063.

[30] Y. Yang, W. Wang, G. Gan, X. Shi, B. Tang, Structural, mechanical and electronic properties of (TaNbHfTiZr)C high entropy carbide under pressure: Ab initio investigation, Physica B 550 (2018) 163–170, https://doi.org/10.1016/j.physb.2018.09.014.

[31] T.J. Harrington, J. Gild, P. Sarker, C. Toher, C.M. Rost, O.F. Dippo, C. McElfresh, K. Kaufmann, E. Marin, L. Borowski, P.E. Hopkins, J. Luo, S. Curtarolo, D.W. Brenner, K.S. Vecchio, Phase stability and mechanical properties of novel high entropy transition metal carbides, Acta Mater. 166 (2019) 271–280, https://doi.org/10.1016/j.actamat.2018.12.054.

[32] B. Ye, T. Wen, M.C. Nguyen, L. Hao, C.-Z. Wang, Y. Chu, First-principles study, fabrication and characterization of $(Zr_{0.25}Nb_{0.25}Ti_{0.25}V_{0.25})C$ high-entropy ceramics, Acta Mater. 170 (2019) 15–23, https://doi.org/10.1016/j.actamat.2019.03.021.

[33] W. Shen, M. Tsai, J. Yeh, Machining performance of sputter-deposited $(Al_{0.34}Cr_{0.22}Nb_{0.11}Si_{0.1}1Ti_{0.22})_{50}N_{50}$ high-entropy nitride coatings, Coatings 5 (2015) 312–325, https://doi.org/10.3390/coatings5030312.

[34] T. Jin, X. Sang, R.R. Unocic, R.T. Kinch, X. Liu, J. Hu, H. Liu, S. Dai, Mechanochemical-assisted synthesis of high-entropy metal nitride via a soft urea strategy, Adv. Mater. 30 (2018) e1707512, , https://doi.org/10.1002/adma.201707512.

[35] K. Johansson, L. Riekehr, S. Fritze, E. Lewin, Multicomponent Hf-Nb-Ti-V-Zr nitride coatings by reactive magnetron sputter deposition, Surf. Coat. Technol. 349 (2018) 529–539, https://doi.org/10.1016/j.surfcoat.2018.06.030.

[36] G. Tallarita, R. Licheri, S. Garroni, R. Orrù, G. Cao, Novel processing route for the fabrication of bulk high-entropy metal diborides, Scr. Mater. 158 (2019) 100–104, https://doi.org/10.1016/j.scriptamat.2018.08.039.

[37] Y. Qin, J. Liu, F. Li, X. Wei, H. Wu, G. Zhang, A high entropy silicide by reactive spark plasma sintering, J. Adv. Ceram. 8 (2019) 148–152, https://doi.org/10.1007/s40145-019-0319-3.

[38] J. Gild, Y. Zhang, T. Harrington, S. Jiang, T. Hu, M.C. Quinn, W.M. Mellor, N. Zhou, K. Vecchio, J. Luo, High-entropy metal diborides: a new class of high-entropy materials and a new type of ultrahigh temperature ceramics, Sci. Rep. 6 (2016) 37946, https://doi.org/10.1038/srep37946.

[39] Y. Zhang, T. Zuo, Z. Tang, M. Gao, K. Dahmen, P. Liaw, Z. Lu, Microstructures and properties of high-entropy alloys, Prog. Mater. Sci. 61 (2014) 1–93, https://doi.org/10.1016/j.pmatsci.2013.10.001.

[40] R. Shi, Y. Pu, W. Wang, Y. Shi, J. Li, X. Guo, M. Yang, Flash sintering of barium titanate, Ceram. Int. 45 (2019) 7085–7089, https://doi.org/10.1016/j.ceramint.2018.12.211.

[41] Y. Zou, H. Ma, R. Spolenak, Ultrastrong ductile and stable high-entropy alloys at small scales, Nat. Commun. 6 (2015) 7748, https://doi.org/10.1038/ncomms8748.

[42] N. Zhou, T. Hu, J. Luo, Grain boundary complexions in multicomponent alloys: challenges and opportunities, Curr. Opin. Solid State Mater. Sci. 20 (2016) 268–277, https://doi.org/10.1016/j.cossms.2016.05.001.

[43] Z. Wang, C. Wang, T. Wang, Y. Xiao, Y. Pu, $Ba(Fe_{0.5}Nb_{0.5})O_3@SiO_2$ core-shell structures with low dielectric loss over a broad frequency and temperature by aqueous chemical coating approach, J. Alloy. Comp. 739 (2018) 190–201, https://doi.org/10.1016/j.jallcom.2017.12.191.

[44] N. Zhou, T. Hu, J. Huang, J. Luo, Stabilization of nanocrystalline alloys at high temperatures via utilizing high-entropy grain boundary complexions, Scr. Mater. 124 (2016) 160–163, https://doi.org/10.1016/j.scriptamat.2016.07.014.

[45] L. Zhang, Y. Pu, M. Chen, T. Wei, X. Peng, Chem. Eng. J. (2020), https://doi.org/10.1016/j.cej.2019.123154.

[46] L. Zhang, Y. Pu, M. Chen, T. Wei, Wade Keipper, R. Shi, Xu Guo, Run Li, Xin Peng, High energy-storage density under low electric fields and improved optical transparency in novel sodium bismuth titanate-based lead-free ceramics, J. Eur. Ceram. Soc. 40 (2020) 71–77, https://doi.org/10.1016/j.jeurceramsoc.2019.09.001.

[47] J. Huang, J. Zhang, H. Yu, M. Wei, H. Chen, C. Yang, Improvement of dielectric and energy storage properties in $BaTiO_3$ ceramics with $BiNbO_4$ modified, Ferroelectrics 510 (2017) 8–15, https://doi.org/10.1080/00150193.2017.1325709.

[48] P. Ge, X. Tang, Q. Liu, Y. Jiang, W. Li, J. Luo, Energy storage properties and electrocaloric effect of $Ba_{0.65}Sr_{0.35}TiO_3$ ceramics near room temperature, J. Mater. Sci. Mater. Electron. 29 (2017) 1075–1081, https://doi.org/10.1007/s10854-017-8008-x.

[49] Y. Zhang, Y. Li, H. Zhu, Z. Fu, Q. Zhang, Sintering temperature dependence of dielectric properties and energy-storage properties in $(Ba,Zr)TiO_3$ ceramics, J. Mater. Sci. Mater. Electron. 28 (2016) 514–518, https://doi.org/10.1007/s10854-016-5552-8.

[50] P. Ren, Q. Wang, S. Li, G. Zhao, Energy storage density and tunable dielectric properties of $BaTi_{0.85}Sn_{0.15}O_3$/MgO composite ceramics prepared by SPS, J. Eur. Ceram. Soc. 37 (2017) 1501–1507, https://doi.org/10.1016/j.jeurceramsoc.2016.12.016.

[51] D. Zhan, Q. Xu, D. Huang, H. Sun, F. Gao, F. Zhang, Effects of composition on dielectric properties of $(Ba,Ca)(Zr,Ti)O_3$ ceramics for energy storage capacitors, J. Electron. Mater. 46 (2017) 4503–4511, https://doi.org/10.1007/s11664-017-5435-7.

[52] L. Zhang, Y. Pu, M. Chen, Influence of $BaZrO_3$ additive on the energy-storage properties of $0.775Na_{0.5}Bi_{0.5}TiO_3$-$0.225BaSnO_3$ relaxor ferroelectrics, J. Alloy. Comp. 775 (2019) 342–347, https://doi.org/10.1016/j.jallcom.2018.10.025.

[53] F. Li, J. Zhai, B. Shen, H. Zeng, X. Jian, S. Lu, Multifunctionality of lead-free $BiFeO_3$-based ergodic relaxor ferroelectric ceramics: high energy storage performance and electrocaloric effect, J. Alloy. Comp. 803 (2019) 185–192, https://doi.org/10.1016/j.jallcom.2019.05.367.

[54] M. Zhou, R. Liang, Z. Zhou, X. Dong, Novel $BaTiO_3$-based lead-free ceramic capacitors featuring high energy storage density, high power density, and excellent stability, J. Mater. Chem. C. 6 (2018) 8528–8537, https://doi.org/10.1039/c8tc03003k.